# Transient Modelling of a Fluorine Electrolysis Cell; Fully Coupled Electric Currents, Heat-Transfer, Diluted Species Transport and Laminar Bubbly Flow

[1,*] Ryno Pretorius, [1]Philip L. Crouse and [2]Christiaan J. Hattingh
[1]University of Pretoria, [2]Metallurgical Testing and Consulting (MTC) cc
*Corresponding author: r.nielater@gmail.com

**Abstract:** A laboratory-scale fluorine reactor was simulated with COMSOL Multiphysics®. This model employs fundamental fully coupled electron-, heat-, mass- and momentum transfer (two-phase) equations to deliver a transient model of the above-mentioned reactor. Quasi-steady-state results were produced for the current density, electric field, temperature, reactive species concentration, gas- and liquid velocity profiles as well as gas fraction distribution within the reactor. Simulation results were verified by modelling and comparing models from published works on similar reactors (Espinasse *et al.*, 2006 and Roustan *et al.*, 1997), as the laboratory-scale reactor is still in construction phase. Favourable comparisons were found. Furthermore a parametric study was also done on the estimated electrolyte thermal conductivity. It is recommended that results of the simulation be used in the design and optimisation of the incomplete laboratory-scale reactor.

**Keywords:** Fluorine production, two-phase simulation, comparative study.

### *List of Symbols*

| | |
|---|---|
| $C_i$ | Concentration of chemical species $i$ ($mol \cdot m^{-3}$) |
| $C_{0,i}$ | Initial concentration of species $i$ ($mol \cdot m^{-3}$) |
| $C_p$ | Heat capacity at constant pressure ($J \cdot kg^{-1} \cdot K^{-1}$) |
| $C_{p0}$ | Heat capacity at constant pressure at 25 °C ($J \cdot kg^{-1} \cdot K^{-1}$) |
| $d_p$ | Average bubble diameter (m) |
| $D_i$ | Isotropic diffusion coefficient for chemical species $i$ ($m^2 s^{-1}$) |
| $E$ | Cell current efficiency (1) |
| $\vec{F}$ | Volume force vector ($kg \cdot s^{-2} \cdot m^{-2}$) |
| $F$ | Faradays constant ($A \cdot s \cdot mol^{-1}$) |
| $g$ | Gravitational acceleration ($m \cdot s^{-2}$) |
| $i$ | Current density ($A \cdot m^{-2}$) |
| $i_n$ | Current density for electrode $n$ ($A \cdot m^{-2}$) |
| $i_0$ | Exchange current density ($A \cdot m^{-2}$) |
| $k_i$ | Electrode $i$ rate constants ($m \cdot s^{-1}$) |
| $k_t$ | Thermal conductivity of electrolyte ($W \cdot m^{-1} \cdot K^{-1}$) |
| $N_i$ | Molar flux of species $i$ in the electrolyte ($mol \cdot m^{-2} \cdot s^{-1}$) |
| $n$ | Stoichiometric factor coefficient (1) |
| $P$ | Pressure (kPa) |
| $p_i$ | Reaction order for anodic species $i$ (1) |
| $Q$ | Internal heat source ($W \cdot m^{-3}$) |
| $q_i$ | Reaction order for cathodic species $i$ (1) |
| $R_i$ | Electrode surface molar flux for species $i$ ($mol \cdot m^{-2} \cdot s$) |
| $r_i$ | Reaction rate of specie $i$ in the electrolyte ($mol \cdot m^{-3} \cdot s$) |
| $s_i$ | Stoichiometric coefficient of species $i$ in electrode reaction |
| $T$ | Temperature of electrolyte ($K$) |
| $t$ | Time (s) |
| $T_0$ | Initial electrolyte temperature ($K$) |
| $T_s$ | Temperature of cooling surface $s$ ($K$) |
| $\vec{u}$ | Velocity vector ($m \cdot s^{-1}$) |
| $z_i$ | Charge number of ionic species $i$ (1) |

### *List of Greek Symbols*

| | |
|---|---|
| $\alpha_i$ | Electron transfer coefficient (1) |
| $\beta$ | Thermal expansion coefficient ($°C^{-1}$) |
| $\varepsilon_r$ | Relative permittivity (1) |
| $\Phi$ | Cell electric potential (V) |
| $\Phi_{0,i}$ | Reference potential of electrode $i$ (V) |
| $\varphi_i$ | Volume fraction of phase $i$ (V) |
| $\Phi_{RV}$ | Reversible cell voltage (V) |
| $\eta_i$ | Viscosity of fluid phase $i$ ($Pa \cdot s$) |
| $\eta_s$ | Surface overpotential (V) |
| $\sigma$ | Electrical conductivity ($S \cdot m^{-1}$) |
| $\mu_{m,i}$ | Ionic mobility of species $i$ ($m^2 \cdot mol \cdot J^{-1} \cdot s$) |
| $\rho$ | Electrolyte density ($kg \cdot m^{-3}$) |
| $\rho_0$ | Electrolyte density at 25 °C ($kg \cdot m^{-3}$) |

## 1. Introduction

Fluorine is produced industrially by electrolysing potassium acid fluoride electrolyte. Control of the process is maintained *via* a black box method and very little is understood about the underlying mechanisms involved. An industrial client requested research within this field, to improve

current practice and understanding of such reactors. The first step is the study of a lab-scale reactor; such a reactor is currently under construction.

The conditions inside the electrolysis reactor make the study of the fluid dynamics dangerous and difficult. A computer simulation of the transfer processes could enable scientists and engineers to better understand the mechanisms involved within the fluorine electrolysis reactor. The fluid dynamic behavior of the laboratory-scale reactor was modelled in COMSOL Multiphysics®. The following transfer processes were modelled and subsequently investigated: Electron-, heat-, mass- and momentum transfer; in the terminology of the software suite: electric currents, heat conduction, transport of diluted species and laminar bubbly flow. All interdependent variables were fully coupled during modeling.

As empirical verification of results was not possible (due to the incomplete laboratory-scale reactor) the modeling procedure was verified by simulating and comparing other, similar simulations with published simulations in the same field, using similar reactor conditions. Published works by Espinasse et al. (2006) and Roustan et al. (1997) were simulated. The publication by Mandin et al. (2009) was used further as justification of the results found by the author.

## 2. Theory

### 2.1 Historical background

Ferdinand Frederick Henri Moissan was the first to produce fluorine gas *via* electrolysis (Groult *et al.,* 2007). Moissan's original cell has been refined over the years, but the fundamental operating principles haven't changed much. Industrial manufacture of fluorine requires the extraction of hydrogen fluoride from fluorspar, the electrolysis of hydrogen fluoride to form fluorine gas, and lastly, purification by a separation step (Klose, 2004). Fluorine, originally no more than a laboratory curiosity, later found industrial scale use in the nuclear industry, specifically in uranium enrichment. Today it is used widely, most commonly in refrigerants and fluoro-polymers (Rudge, 1971).

### 2.2 Cell Operation

The basic operation of an electrolysis cell requires a molten potassium-acid-fluoride electrolyte ($KF{\cdot}2HF$, 40.8 % HF) to be subjected to an electric field (Groult, 2003). Potassium-acid-fluoride electrolyte is used due to the low electrical conductivity of hydrogen fluoride. The thermal conductivity of the electrolyte is not widely known and was estimated using the thermal conductivity of potassium fluoride. Hydrogen forms on the cathode and fluorine on the carbon anode. A separator skirt is placed between the electrodes to prevent explosive recombination of the product gasses (Shia, 2005).

Bubble formation and motion are the major sources for fluid flow in the electrolysis cell. The hydrodynamic properties of the electrolyte and the efficiency of the electrolysis reaction are strongly coupled with the flow of bubbles in the reactor. This is also true for diluted species transport and electrical performances due to the stirring effect of bubble motion and the high resistivity of bubbles compared to that of the electrolyte (Mandin *et al.*, 2009).

Thermodynamic *HF* decomposition requires a potential of 2.9 V, but an anode-cathode voltage of 8-10 V is required to maintain a current density of 10-12 $A{\cdot}dm^{-2}$ in industrial cells (Groult, 2003). The reversible cell voltage ($\Phi_{RV}$) or thermodynamic decomposition voltage is the minimum potential required for product formation during electrolysis. Any voltage supplied that surpasses the reversible voltage (done to achieve the desired current density) produces heat through Ohmic heating (Rudge, 1971, Heitz & Kreysa, 1986).

### 2.3 Published Fluorine Electrolysis Simulations

A study was conducted on two publications concerning the simulation of fluorine electrolysers. In an attempt to verify the modelling techniques used by the author simulation will be compared to these results. The reader is encouraged to study the relevant articles if further details are required

The first comparative study was done on a publication by Roustan et al. (1997). In this contribution Flux-Expert® was used to model momentum-, electron- and heat transfer in a typical fluorine electrolyser. Results of the temperature distribution within the cell are shown in Figure 1. Only the temperature results are shown as the incorporate electron transfer (to generate heat) and momentum

transfer (to aid in convection). The results matched up well with experimental measurements once the thermal conductivity was modified to (20 $W \cdot m^{-1} \cdot K^{-1}$). This was a necessary modification due to the electrolyte becoming trapped between the anode and right cathode, a side effect of a two dimensional model. This effect would be less significant in a three dimensional simulation as the electrolyte can move perpendicular to the simulated surface.

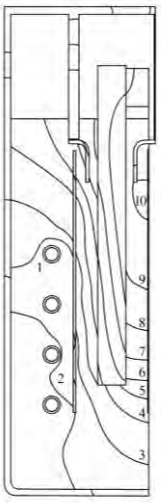


Figure 1: Temperature profile within the electrolyser. Key: (1) 325 *K*; (2) 332 *K*; (3) 339 *K*; (4) 346 *K*; (5) 353 *K*; (6) 360 *K*; (7) 367 *K*; (8) 374 *K*; (9) 381 *K*; (10) 388 *K*. Reproduced from Roustan et al. (1997).

A second publication by Espinasse et al. (2006) was studied to compare two phase momentum transfer results. The authors used Flux-Expert® (FE) and Estet Astrid (EA) as a modeling platform. Momentum transfer was simulated; the model used heat-, and electron transfer data from previous studies and assumed these values would remain constant. Results are shown in

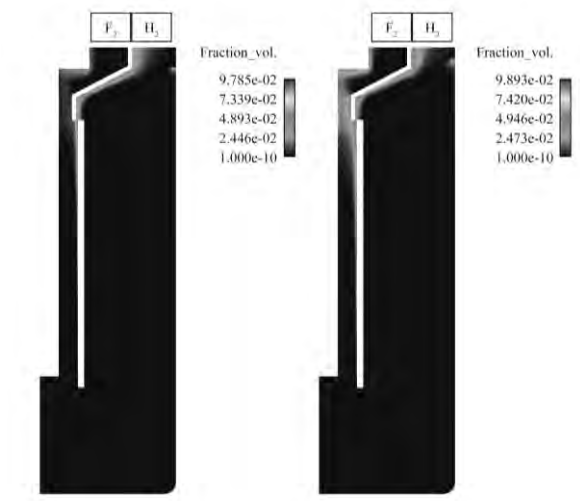


Figure 2.

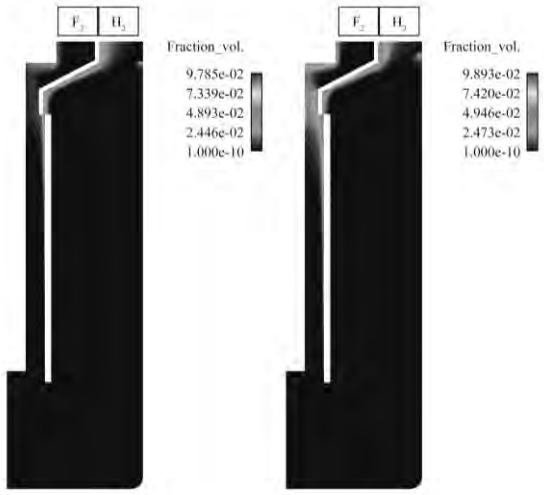


Figure 2 shows a well-developed hydrogen plume in both cases, with a higher gas fraction in the case of a higher current density. In both cases it is clear that there is hydrogen ingress into the fluorine compartment. It is clear that a higher current density leads to more hydrogen ingress.

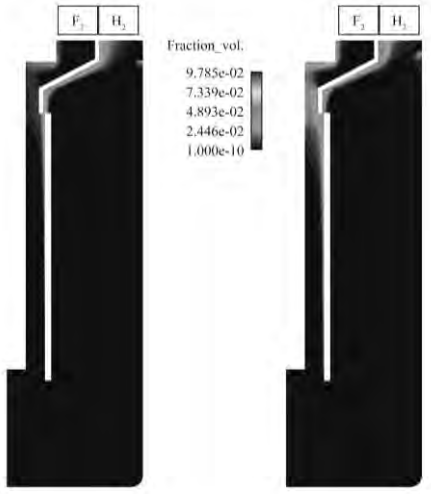


Figure 2: Mean hydrogen gas distribution for two different current densities low on the left and high on the right. Reproduced from Espinasse et al. (2006).

## 3. Modelling in COMSOL Multiphysics®

The model cross section of the fluorine electrolysis cell currently under construction at the University of Pretoria is shown in Figure 3.

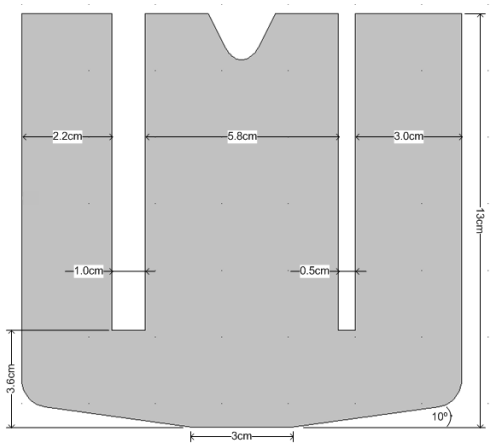


Figure 3: Electrolyte cross-section modelled in COMSOL Multiphysics®.

### 3.1 Electron Transfer

Electron transfer is modelled using the "Electric Currents" physics option. The chemical reaction (electrolytic decomposition of the electrolyte into $F_2$ and $H_2$) is induced by electric potential as prescribed by Equation 1 (Laplace Equation) which models the primary current distribution and adheres to the assumption of Equation 2. Current density distribution is modelled using Equation 3 and Equation 4.

$$-\nabla \cdot d(\sigma \nabla \Phi) = 0 \quad (1)$$

$$\nabla \Phi^2 = 0 \quad (2)$$

$$i = i_0 \left[ \exp\left( \frac{\alpha_A F}{R_g T} \eta_s \right) - \exp\left( \frac{\alpha_C F}{R_g T} \eta_s \right) \right] \quad (3)$$

$$i_0 = F \cdot k_c^{0.5} k_a^{0.5} C_{HF_2^-}^{0.5} C_{HF}^{0.5} \quad (4)$$

The physics model used assumes that the electric field only varies in two dimensions and is constant in the perpendicular direction. By implication the electric filed is tangential to the modelled-plane (COMSOL Multiphysics (c), 2010, Roustan *et al.,* 1997).

### 3.2 Heat Transfer

Heat transfer due to convection and conduction inside the reactor is modelled using the "Heat Transfer (in fluids)" physics option. Equation 5 below (COMSOL Multiphysics (b), 2010, Çengel, 2006) is used to model heat transfer. Heat generation due to viscous heating was ignored. Heat generation in the cells are modelled using Equation 6 (Rudge, 1971).

$$\rho C_p \frac{\partial T}{\partial t} + \nabla \cdot (-k \nabla T) = Q - \rho C_p \vec{u} \nabla T \quad (5)$$

$$Q = i \cdot (\Phi - \Phi_{RV}) + i \cdot \left[ 2.81 \cdot \frac{(100 - E)}{100} \right] \quad (6)$$

### 3.3 Mass Transfer

Mass transfer inside the reactor is modelled using the "Transport of Diluted species" physics option. Equation 7 models mass transfer (Newman, 1991: 194, Welty *et al., 2001,* COMSOL Multiphysics (d), 2010). It was chosen to ensure that the effects of electric field migration, convection, conduction and reaction of ionic species can be taken into account.

$$\frac{\partial C_i}{\partial t} + \nabla \cdot (-D_i \nabla C_i - z_i \mu_{m,i} F C_i \nabla \Phi + C_i \vec{u}) = r_i \quad (7)$$

The three species assumed to be in solution are given in Table 1. The electrolyte dissociation reaction is given by Equation 8 and the anode and cathode half-reactions by Equation 9 and Equation 10 respectively (Groult *et al.*, 2007).

$$KF \cdot 2HF \rightarrow K^+ + HF + HF_2^- \quad (8)$$

$$HF_2^- \rightarrow HF + \tfrac{1}{2} F_2 + e^- \quad (9)$$

$$2HF + e^- \rightarrow HF_2^- + \tfrac{1}{2} H_2 \quad (10)$$

Table 1: Chemical species assumed to be present during the electrolytic process.

| Species | Charge Number ($z_i$) |
|---|---|
| $K^+$ | +1 |
| $HF$ | 0 |
| $HF_2^-$ | -1 |

Dilute species flux at the electrodes was further modified to include the effect of bubbles on the electrode surface. This was implemented by coupling the calculated dilute species flux and liquid fraction (through multiplication) at the electrode boundary.

### 3.4 Momentum Transfer

Flow induced inside the reactor was modelled by Equation 11, Equation 12 and Equation 13 from the "Laminar Bubbly flow" physics option; representing the momentum transport, continuity and laminar bubbly flow equations respectively.

$$\phi_l \rho_l \frac{\partial \vec{u}_l}{\partial t} + \phi_l \rho_l \cdot \nabla \vec{u}_l = -\nabla P + \nabla \cdot \left[ \phi_l (\eta_l + \eta_T) \left( \nabla \vec{u}_l + \nabla \vec{u}_l{}^T - \frac{2}{3} (\nabla \cdot \vec{u}_l) \vec{I} \right) \right] + \phi_l \rho_l g + \vec{F} \quad (11)$$

$$\nabla \cdot \vec{u}_l = 0 \quad (12)$$

$$\frac{\partial \rho_g \phi_g}{\partial t} + \nabla \left( \phi_g \rho_g \vec{u}_g \right) = 0 \quad (13)$$

Subscripts "$l$" and "$g$" denote the gas and liquid phases. The following assumptions are adhered to (COMSOL Multiphysics (a), 2010, Espinasse *et al.,* 2006, Loth *et al.,* 2006):

- The gas density is negligible compared to the liquid density.
- The motion of the gas bubbles relative to the liquid is determined by a balance between viscous drag and pressure forces.
- The two phases share the same pressure field.
- Gas volume fraction is less than 0.1.

### 3.5 Starting and Boundary Conditions

The starting conditions for the reactor is given in Table 2.

Table 2: Starting conditions used in the model.

| **Transfer Process** | **Description** |
|---|---|
| Electron Transfer | Cell Voltage equals 0 V. |
| Heat Transfer | Reactor temperature equals 80 °C. |
| Mass Transfer | Reactive species concentration equals 2000 $mol \cdot m^{-3}$. |
| Momentum Transfer | Velocity equals zero. |

Boundary conditions used in the model are given in Table 3. Representing electron-, heat-, mass- and momentum transfer boundary conditions respectively.

Table 3: List of parameters and expressions used during simulation.

| Boundary | Condition |
|---|---|
| Anode surface | Gas flux specified. Thermal insulation. Specified current density. |
| Cathode surface | No slip for liquid flow. Gas flux specified. Thermal insulation. Specified current density. |
| Cooling walls | No slip for liquid. Temperature specified as $T_W$. Electrical insulation. |
| Electrolyte level | No electron or heat flow permitted (insulation). Slip condition for liquid flow. |
| Other boundaries | Thermal and electrical insulation. Liquid no slip condition. |

A list of constants used during modelling is given in Table 4. Empirical equations used in the modelling procedure are given in Table 5.

Table 4: Model constants

| Constant | Value |
|---|---|
| $C_{p0}$ | 10.8 $J \cdot kg^{-1} \cdot K^{-1}$ |
| $d_b$ | 1 mm |
| $D_{HF}$ | $2.8 \times 10^{-5}$ $m^2 s^{-1}$ |
| $D_{HF2-}$ | $3 \times 10^{-5}$ $m^2 s^{-1}$ |
| $E$ | 95 % |
| $k_t$ | 1.25 $W \cdot m^{-1} \cdot K^{-1}$ |
| $k_A$, $k_C$ | 10 $m \cdot s^{-1}$ |

| | |
|---|---|
| $T_0$, $T_w$ | 353,15 $K$ |
| $\alpha_A$, $\alpha_C$ | 0.5 |
| $\beta$ | $7.11\times10^{-4}$ °C$^{-1}$ |
| $\varepsilon_r$ | 9 |
| $\Phi$ | 12 V |
| $\Phi_{RV}$ | 1.9 V |
| $\Phi_{0,A}$ | 2.9 V |
| $\Phi_{0,C}$ | 0 V |
| $\eta_l$ | 0.0113 Pa·s |
| $\eta_g$ | 0.001 Pa·s |
| $\rho_0$ | 2000 kg·m$^{-3}$ |
| σ | 6.67 S·m$^{-1}$ |

Table 5: Modelling Equations.

| Variable | Expression |
|---|---|
| $C_p$ | $C_p = C_{p0} + 0.00284 \cdot T$ |
| $Q$ | $Q = i \cdot (\Phi - 1.9V) + i \cdot \left[ 2.81 \cdot \frac{(100-95)}{100} \right]$ |
| $R_A$ | $R_A = -\frac{1}{F} i_A$ |
| $R_C$ | $R_C = -\frac{2}{F} i_C$ |
| $i_0$ | $i_0 = F \cdot k_c^{0.5} k_a^{0.5} C_{HF_2^-}^{0.5} C_{HF}^{0.5}$ |
| $i_A$ | $i_A = i_0 \left[ \exp\left( \frac{\alpha_A F}{R_g T} \eta_s \right) - \exp\left( \frac{\alpha_C F}{R_g T} \eta_s \right) \right]$ |
| $i_C$ | $i_C = -i_0 \left[ \exp\left( -\frac{\alpha_A F}{R_g T} \eta_s \right) - \exp\left( -\frac{\alpha_C F}{R_g T} \eta_s \right) \right]$ |
| $\eta_{s,A}$ | $\eta_{s,A} = \Phi - \Phi_{0,A}$ |
| $\eta_{s,C}$ | $\eta_{s,C} = -\Phi - \Phi_{0,C}$ |
| $\rho$ | $\rho = \rho_0 \cdot (\exp(\beta(T - 25^\circ C)))^{-1}$ |

### 3.6 Mathematical Solution

#### 3.6.1 Solution Method – Study sequences

MUltifrontal Massively Parallel sparse direct Solver (MUMPS) was used as a direct solver and a Backward Differentiation Formula (BDF) for time stepping.

To solve the electron transfer problem (Calculation A) cell potential (Ecell) was used as a changing parameter in a separate stationary parametric sweep calculation step. The value of Ecell was incrementally increased form 3 V to 12 V. This allowed the simulation to use the lower (and easier to solve) value of Ecell as a starting point for the next (higher value).

The final 12 V value of Ecell was then used as a starting value input to a time dependent calculation (Calculation B). In this second calculation the momentum- and heat-transfer phenomena were solved, based on the constant electron transfer values supplied. Momentum and electron-transfer was chosen due to their coupling and large amounts of interaction.

A third calculation (Calculation C) was attempted, where the results of Calculation B were used as initial input values. In this calculation the mass-transfer in the reactor was calculated, using the values calculated in Calculation B. Mass-transfer was calculated last as it is coupled with all the other transfer modules and presents a significant challenge to the solver.

It is clear that final calculation (Calculation D) was needed to firstly determine time dependent values of all transfer phenomena and to also ensure transient coupling between all transient transfer regimes. In this calculation electron-, mass- momentum and heat-transfer was calculated. It was chosen last as it is the largest and most complex set of equations to solve, where coupling occurs between all transfer modules. In Calculation C stationary values of electron transfer and transient values of heat, momentum- and ion-transfer was used to solve for transient values of mass transfer. To achieve calculation D calculation C was used as an initial value input. Results of Calculation D are presented in the Results and Discussion section. Calculation D includes fully coupled time dependent ion-transfer results.

#### 3.6.2 Mesh

An overall “finer” qualitative mesh setting was applied to the model. The mesh was further refined around the electrodes and separator skirt, where steeper gradients in the solution of several quantities were expected, specifically in terms of current density concentrations.

Further statistics concerning the mesh is presented in Figure 4. As an additional step to ensure the reliability of the solution, a further study was conducted, to ensure that the solution obtained is not a mesh dependent solution. The size of mesh elements was decreased: It was found that the solution was practically identical for each mesh size and therefore it can be concluded that the solution is not mesh dependent.

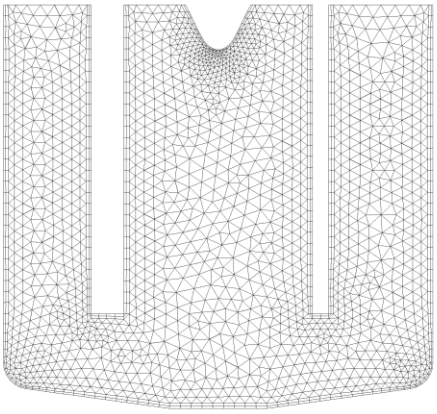

Figure 4: Meshing framework of fluorine cell.

## 4. Results and discussion

A quasi-steady-state approach was followed by Espinasse *et al.*, (2006) where it was assumed that there would be very little change in the flow patterns of the reactor once the bubble plume had fully formed. The same assumption was made in this contribution. Results shown are at 100 s (by evaluation of results the quasi-steady-state has been reached at this time).

In general arrows represented in results indicate direction and is proportional to the norm of the vector quantity represented, at the arrow starting point. Furthermore; colours indicate values as given by the legend to the right of the image.

### 4.1 Electron Transfer

The normal current density distribution inside the electrolysis reactor can be seen in Figure 5. The colour scale represents current density in $A \cdot m^{-2}$. This figure also contains streamlines indicating electric field lines between the electrodes.

High current densities appear on sharp corners of the electrodes; especially high values are visible on tips between the two electrodes. Current density is also very high on the tip of the separator skirt. The tip of the skirt exhibits high current density values due to the fact that electrons flow around this point to travel between electrodes. These locations are then also the major contributors in Ohmic heating of the cell during electrolysis.

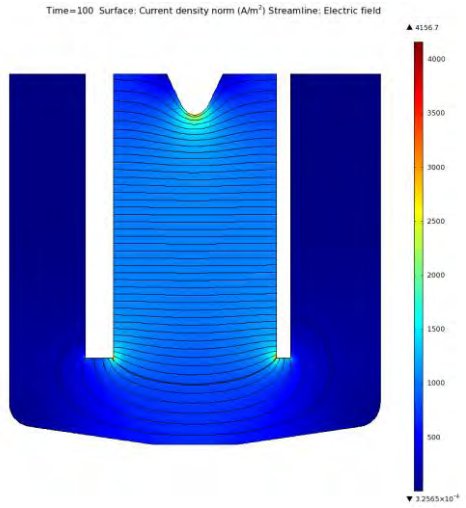


Figure 5: Current density distribution and electric field streamlines.

Current density variation along the anode is shown in Figure 6. The "Arc Length" axis starts at the top left of the anode and ends at the top right.

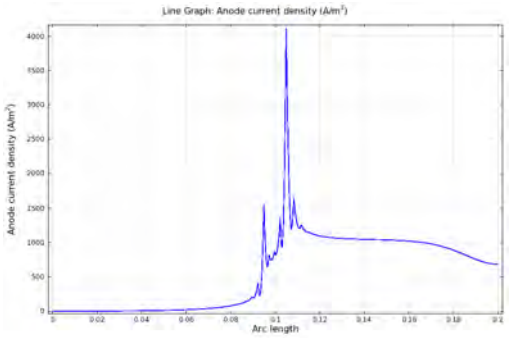


Figure 6: Anode current density variation along the electrode.

From Figure 6 it is clear that the current density is exceptionally high at the tips of the electrode. This caused some difficulty during the mathematical solution procedure. The current density spikes serve as a virtual discontinuity when moving between mesh nodes, making it difficult for the Newtonian solver to find a solution. The problem was overcome by refining the mesh around the high current density areas and by decreasing the size of steps taken by the solver. In physical reactors these current density spikes can lead to electrode degradation in the reactor, and as such the simulation is in agreement with empirical findings in general. The mirror of this image (Cathode Current Density Variation) is not shown here.

Figure 7 shows the electric potential and electric potential contour lines. The colour scale indicates electric potential in V. Electric potential drops from the anode to the cathode from 9.1 V and 0 V as expected. This result corresponds to the potential change expected from the literature.

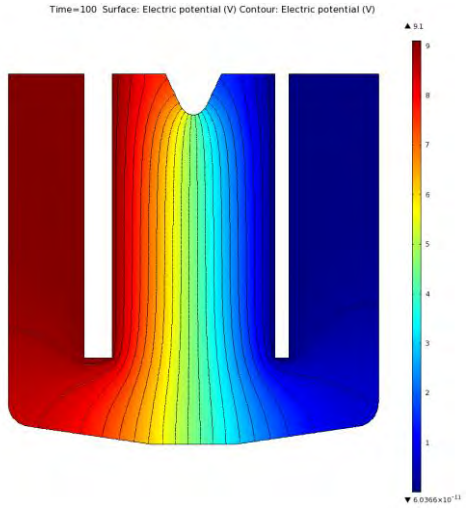


Figure 7: Electric potential plot.

## 4.2 Heat Transfer

The temperature distribution inside the reactor is shown in Figure 8; the colour scale on the right indicates temperature in *K*.

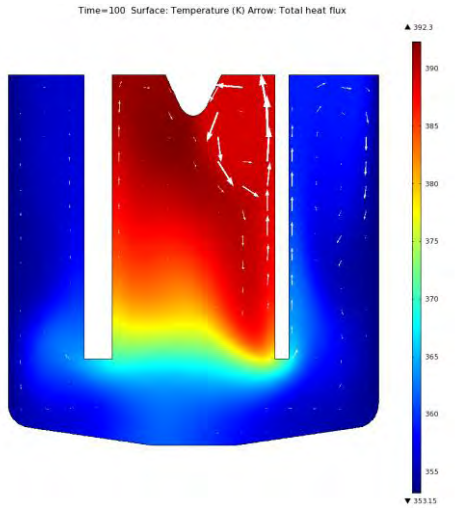


Figure 8: Heat flux and reactor temperature profile.

Ohmic heating is the major source of reactor heating as reflected by the current density concentration seen in Figure 5. The stirring effect of the moving liquids, induced by the moving gases, and shown by the vector arrows are visible in Figure 8. The heat flux arrows indicate that convection is the dominant heat transfer contributor, as heat flux resembles electrolyte motion. The cooling effect of the reactor walls can also be seen as the temperature decreases closer to the cooled wall.

### 4.2.1 Parametric Study

A parametric study (results can be seen in Figure 9) of electrolyte thermal conductivity versus the temperature profile in the reactor was done.

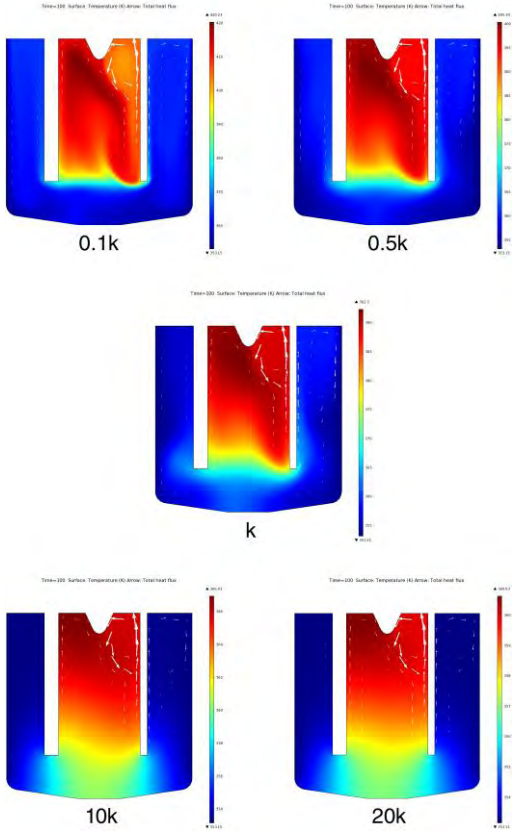


Figure 9: Parametric study images, showing change in temperature with a change in thermal conductivity.

Thermal conductivity was chosen as it has a significant influence on the temperature distribution within the reactor. Temperature is further coupled to electron-, mass- and momentum transfer. Further reasons include:

- The value of thermal conductivity used in the initial simulations was estimated from the value of the thermal conductivity of potassium fluoride as it is not widely known.
- Work by Roustan et al. (1997) also indicated the importance of the thermal conductivity term during simulation.

Scale factors chosen for thermal conductivity was: 0.1, 0.5, 10, and 20.

Results from the parametric study show that the maximum temperature as well as the heat distribution in the reactor varies with a change in thermal conductivity. It is however noted that even an increase in thermal conductivity by a factor of 20, changes the maximum reactor temperature by less than 32 *K*. The same can be said for lowering the conductivity by a factor of 10, a maximum temperature increase of only 26 *K*. It was observed that an increase in thermal conductivity leads to a more symmetric temperature distribution (as can be expected).

### 4.3 Mass Transfer

HF concentration in $mol \cdot m^{-3}$ is shown in Figure 10.

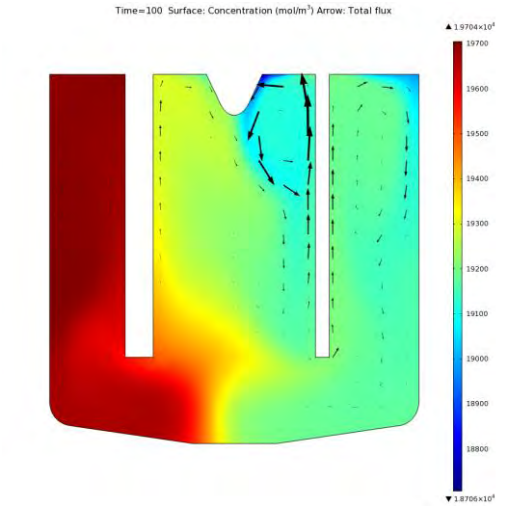


Figure 10: Dissolved hydrogen fluoride flux and flux vectors.

HF is produced at the anode and consumed at the cathode. The concentration gradient due to consumption at the cathode is a contributor to flux in the form of diffusion. From the scale-bar on the right it is clear that more HF is consumed than produced, as was predicted by the electrode half-reactions (Equation 9 and Equation 10). From Figure 10 it is evident that the secondary contributors to flux are convection and migration due to electric field.

$HF_2^-$ ion-flux and concentration (not shown) is a mirror image of Figure 10. The $HF_2^-$ ion is produced at the cathode and consumed at the anode. The concentration gradient indicates ion-flux from the cathode to the anode as expected. Convection is evident as the major contributor to ion-flux in the simulation, with diffusion due to concentration gradient and migration due to electric field acting as secondary contributor.

### 4.4 Momentum Transfer

Gaseous movement inside the reactor can be seen in Figure 11. The colour scale on the right indicates gaseous velocity in $m \cdot s^{-1}$. It should be noted that the arrows do not indicate the presence of gas, but only the vector velocity a bubble would have at that point in a reactor.

From Figure 11 it is clear that gas is produced at both electrodes. The product gasses move away from the electrodes, upwards and out of the reactor. This upward motion contributes to the liquid phase movement inside the reactor.

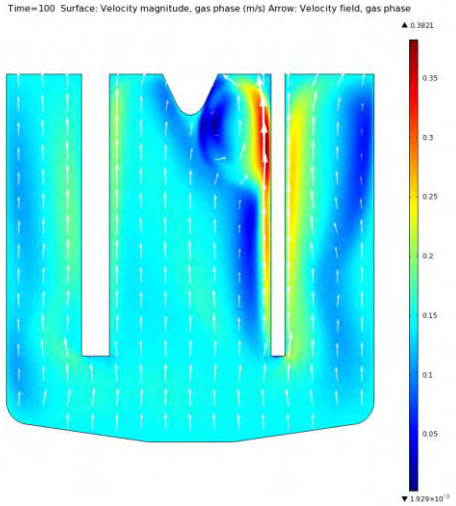


Figure 11: Gas phase velocity inside the electrolysis reactor.

Liquid phase movement can be seen in Figure 12. The colour scale on the right represents liquid phase velocity inside the reactor, warmer colours represent higher velocities.

The liquid movement induced by gaseous (specifically hydrogen) movement is evidenced by the swirling liquid phase eddy between the separator skirt and the cathode at the top right of the reactor. This same eddy has the effect of causing stirring throughout the reactor. This aligns well with what is observed in industrial and other lab-scale reactors.

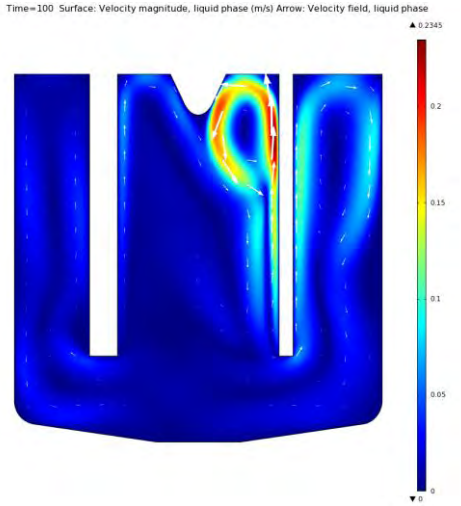


Figure 12: Liquid phase velocity inside the reactor.

Liquid velocity and gas fraction in the reactor are shown in Figure 13.

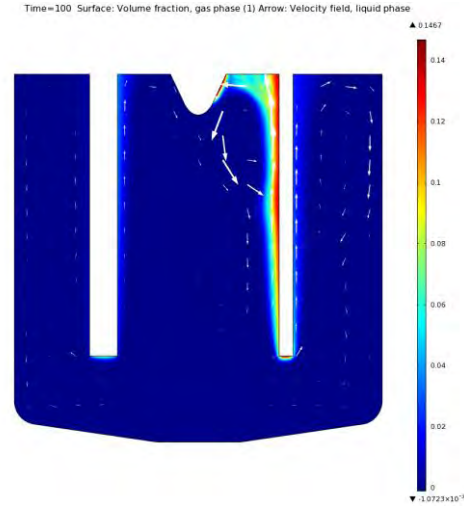


Figure 13: Gas phase fraction in the reactor.

Figure 13 shows a well-developed hydrogen plume and detachment from the cathode occurs as expected. The fluorine plume on the other hand does not detach from the anode. This is to be expected as fluorine bubbles form long lenticular bubbles that tend to move slowly up along the electrode. Very little hydrogen migration into the fluorine section is observed; therefore the chance of explosive recombination of product gasses is very low. This is also good news from a productivity standpoint, as fewer product gases are lost and less purification of product streams will be required.

### 4.5 Simulations of Published Results

This section contains the results of the authors' attempts to simulate published results using COMSOL Multiphysics®. Simulations used parametric data as supplied, when available in a publication. Assumptions based on the author's parametric data were made where parametric data concerning the individual cells was unavailable. Specialised correlations and equations used in published works that could not be reproduced were supplemented with the modelling procedure as described in section 3.5 of this report.

#### 4.5.1 Modelling coupled transfers in an industrial fluorine electrolyser (Roustan et al., 1997)

The resulting equipotential curve is shown in Figure 14. When comparing the equipotential curves to those by Roustan and co-workers a similar voltage drop between the electrodes was found.

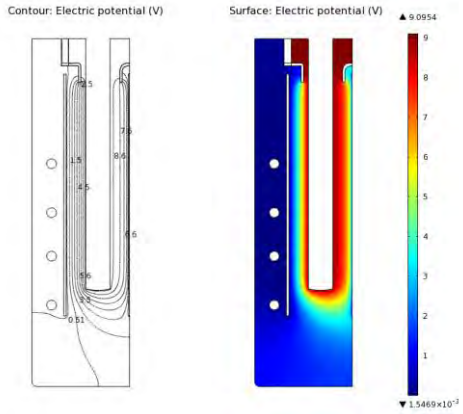


Figure 14: Equipotential curves from the COMSOL simulation of the cell as published by Roustan et al., (1997).

The electric potential gradient obtained in the first simulation was then used as initial condition for a coupled simulation with heat transfer – results in Figure 15. The model further implements a coupled velocity profile model as induced by thermal differences throughout the reactor (not shown).

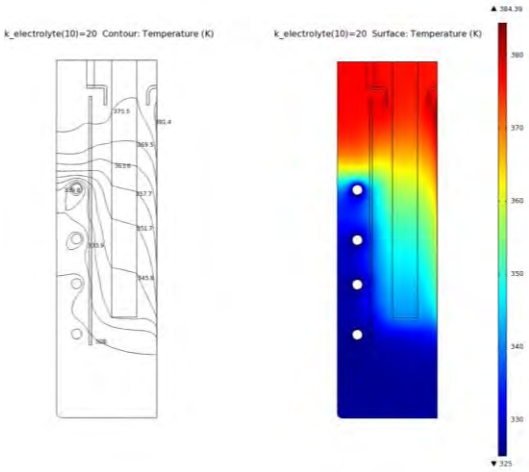


Figure 15: Temperature profiles inside the reactor as simulated in COMSOL.

Similar deviations as observed by Roustan and co-workers in terms of thermal conductivity were observed: k=1.25 $W \cdot m^{-1} \cdot K^{-1}$ resulted in a maximum temperature much higher than empirical measurements. A thermal conductivity value of 20 $W \cdot m^{-1} \cdot K^{-1}$ (as used by Roustan et al., 1997) practically eliminates the deviation (as seen in Figure 15). The Roustan simulation also incorporates radiative heat losses. This was not done by the author, as it increases computational complexity without adding significantly to the simulated results.

### 4.5.2 Effect of hydrodynamics on Faradaic current efficiency in a fluorine electrolyser (Espinasse et al., 2006)

The result of the first simulation is presented in Figure 16. Gas fraction shown is the gas fraction of hydrogen. The hydrogen flow rate was so chosen was to ensure a similar hydrogen plume shape as that obtained by the Espinasse group. A comparison can be drawn between Figure 16 and

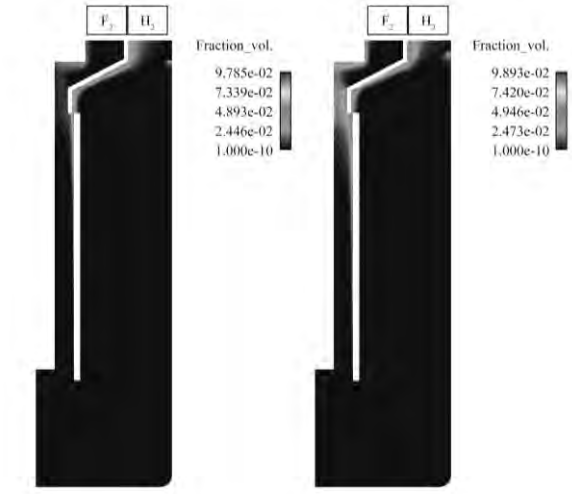


Figure 2. Assessment of the two sets of results shows a similar hydrogen plume but significantly higher gas fractions when compared to those of the Espinasse group. There is also significantly more overflow of hydrogen into the fluorine compartment

In the publication by Mandin *et al.*, (2009) a bubble plume in a water solution can clearly be observed. It is expected that a hydrogen plume in a fluorine electrolyser has the same shape and gas fraction, therefore the shape obtained by Espinasse et al. (2006) and this author's simulations should be correct. It does however cast some doubt on the gas fraction values obtained in the Espinasse publication.

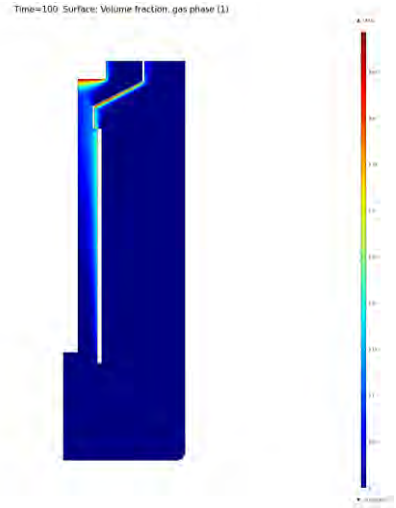


Figure 16: COMSOL simulation of published (Ibid.) electrolyser.

## 5. Conclusions and Recommendations

### 5.1 Experimental Design Simulation

Results obtained, under the quasi-steady-state assumption, from the simulations are reasonable and within expectations. All comparative simulations also deliver satisfactory results, when compared the published works.

Current density and electric potential field lines predictions correspond to expectations match up satisfactorily with those found by Roustan et al. (1997). It is however recommended that the fluorine production kinetics be investigated to deliver more accurate mass transfer results in future.

It can be concluded that convection is the major contributor to heat transfer. The thermal conductivity value used ($1.25\ W \cdot m^{-1} \cdot K^{-1}$) is sufficiently accurate according to the parametric study. The temperature distribution within the cell is within expected limits, the high value found when solving the Roustan et al. (1997) simulation can be rectified in a similar way. As with heat transfer, it was found that convection is the major cause of mass transfer within the simulated reactor. It was found that the simulation of the incomplete reactor did not suffer from the same heat transfer difficulties experienced by the Roustan group, due to geometric differences that enhance mixing capability.

The simulated results show a strong correlation between the gaseous phase movement (induced by buoyancy forces) and that of the liquid phase. The gas-phase flux seen in Figure 13 shows that little or no hydrogen gas transfers to the fluorine compartment. The shape of the gaseous plume of hydrogen that forms at the anode has the same shape as that published in literature when compared to the results from Espinasse et al. (2006) and Mandin et al. (2009). There is however a difference in the gaseous fraction between the published and simulated reactors.

## 6. References


Çengel, YA (2006) Heat and Mass Transfer, McGraw-Hill, Singapore.

COMSOL Multiphysics (a), Chemical Engineering Modules User's Guide, Bubbly Flow, Version 4.0, 164-173 (April 2010). COMSOL and COMSOL Multiphysics are registered trademarks of COMSOL AB.

COMSOL Multiphysics (b), Heat Transfer Modules User's Guide, Theory of Heat Transfer, Version 4.0, 1-14 (April 2010). COMSOL and COMSOL Multiphysics are registered trademarks of COMSOL AB.

COMSOL Multiphysics (c), AC/DC Modules User's Guide, Fundamentals of Electromagnetics, Version 4.0, 40-46 (April 2010). COMSOL and COMSOL Multiphysics are registered trademarks of COMSOL AB.

COMSOL Multiphysics (d), Chemical Engineering Modules User's Guide, Transport of Diluted Species, Version 4.0, 253-268 (April 2010). COMSOL and COMSOL Multiphysics are registered trademarks of COMSOL AB.

Espinasse, G, Peyrard, M, Nicolas, F and Caire JP (2006) "Effects of hydrodynamics on Faradaic current efficiency in a fluorine electrolyser" *Journal of Applied Electrochemistry* (2007) 37:77-85.

Groult, H, Devilliers, D (2000) "Fluorine evolution at carbon/KF-2HF interface" *Journal of Fluorine Chemistry*, 263-267.

Groult, H (2003) "Electrochemistry of Fluorine Production" *Journal of Fluorine Chemistry*, 119 173-189.

Groult, H, Lantelme, F, Salanne, M, Simon, C, Belhomme, C, Morel, B, Nicolas, F (2007) "Role of Elemental Fluorine in Nuclear Field" *Journal of Fluorine Chemistry*, 128 285–295.

Heitz, E and Kreysa G (1986) Principles of Electrochemical Engineering, VCH Verslasgesellschaft mbH, Weinheim.

Rudge, AJ (1971) "Production of elemental fluorine by electrolysis", Industrial Electrochemical Processes, Kuhn, A (Editor), Elsevier Publishing Company, Amsterdam.

Klose, F (2004) "Elements and Compounds, Atoms and Molecules – Structures and Bonds", Course on Inorganic Chemistry for the University of Magdeburg, Magdeburg.

Loth, E, Tryggvason, Y, Tsuji, Y, Elghobashi, SE, Clayton, Crowe, CT, Berlemond, A, Reeks, M, Simonin, O, Frank, Th, Onishi, Y and van Wachen, B (2006) "Modeling", in Multiphase Flow Handbook, Chapter 13, Crowe, CT (Editor-in-Chief), Taylor & Francis Group, Florida.

Mandin, Ph, Wüthrich, R and Roustan, H (2009) "Electrochemical Engineering Modelling of the Electrodes Kinetic Properties During Two-Phase Sustainable Electrolysis" 10th International Symposium on Process Systems Engineering

Newman, JS (1991) Electrochemical Systems, Prentice Hall, New Jersey.

Roustan, H, Caire, JP, Nicolas, F, Pham, P (1997) "Modelling coupled transfers in an industrial fluorine electrolyser" Journal of Applied Electrochemistry, 28 (1998) 237 243.

Shia, G (2005) "Fluorine", in Kirk-Othmer Encyclopedia of Chemical Technology, 14, Seidel Arza (Editor-in-Chief), John Wiley & Sons, Inc., New Jersey.

Welty, JR, Wicks, CE, Wilson, RE, Rorrer, GL (2001) *Fundamentals of Momentum, Mass and Heat Transfer 4th Edition*, John Wiley and Sons, Inc., United States of America.